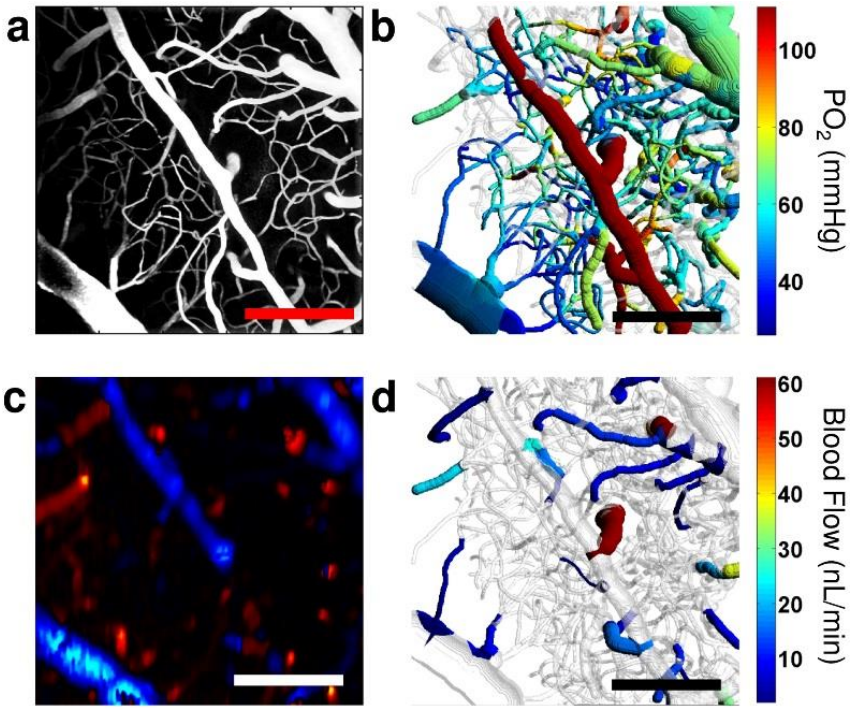

Supplementary Figure 1: Co-registration of the Two-Photon Microscopy and OCT data. (**a**) Maximum intensity projection (MIP) of the 200-µm-thick cortical microvascular stack obtained by TPM. Blood plasma was labeled by FITC. (**b**) Top-view projection of the segmented microvasculature with the intravascular PO_2 measurements obtained by TPM. Mean vascular segment PO_2 measurements were color-coded and overlaid on the segmented microvascular structure. (**c**) MIP of the OCT image of the red blood cell velocity projections to the microscope optical axis in the upper 150-µm-tick segment of the microvasculature. The OCT data was previously co-registered with the vascular stack in **a**. (**d**) Top-view projection of the segmented microvasculature obtained by TPM, with the co-registered OCT measurements of the blood flow. Measured blood flow values in penetrating arterioles and surfacing venules were color-coded and overlaid on the segmented microvascular structure. Scale bars, 200 µm.

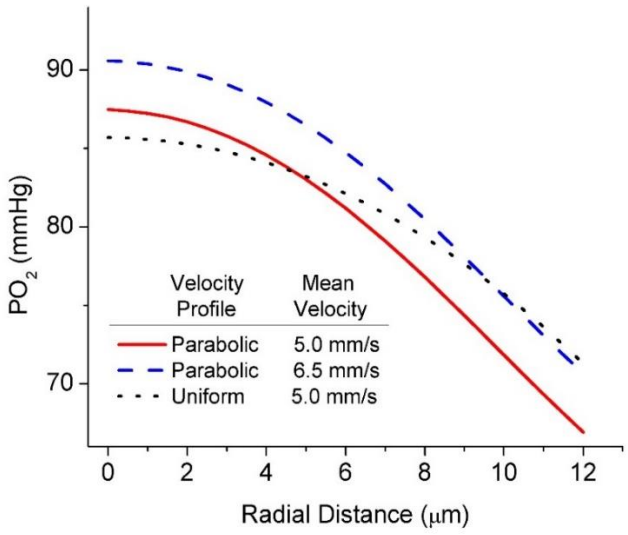

Supplementary Figure 2: Simulated intra-arteriolar PO_2 radial profiles. Simulated intra-arteriolar radial PO_2 profiles in an arteriole with a 24 μm diameter. PO_2 profiles were calculated 100 μm downstream from the place where the fresh blood (PO_2 = 100 mmHg) enters the vessel. The radial blood velocity distribution was independent of position along the vessel axis. We considered three velocity distributions: 1) parabolic distribution with mean blood velocity 5 mm s^{-1} (solid red line); 2) parabolic distribution with mean blood velocity 6.5 mm s^{-1} (dashed blue line); 3) uniform distribution with blood velocity 5 mm s^{-1} (dotted black line). Numerical simulations of a steady state oxygen advection and diffusion inside the blood vessel were performed following the procedure described in Kobayashi et al.[1] Other parameters assumed in simulation were: oxygen diffusivity $D = 2 \cdot 10^{-5}$ cm^2 s^{-1}; oxygen solubility α = 1.39 μM $mmHg^{-1}$; hematocrit H = 30%; constant oxygen flux through the vessel wall $J = 6.6 \cdot 10^{-4}$ μmol cm^{-2} s^{-1} (J was estimated by assuming infinitely thin and permeable vessel wall, tissue metabolic rate of oxygen $CMRO_2$ = 2 μmol cm^{-3} min^{-1}, and radius of tissue supplied by the vessel R_t = 70 μm).

While the oxygen release from the vessel is primarily responsible for the concavity of the intravascular PO_2 radial distribution, the exact shape of the PO_2 distribution is influenced by both the blood velocity amplitude and radial profile. For a vessel diameter comparable to the measured arteriolar diameters (**Fig. 2**), changes in blood velocity radial profiles seem to be more influential on the PO_2 distribution shape than changes in the mean blood velocity. We calculated ΔPO_2 = 22.5 mmHg between vessel axis and vessel wall in the case of parabolic blood flow profile and ΔPO_2 = 14.4 mmHg in a case of uniform blood flow profile (a 43% increase in ΔPO_2 due to parabolic flow profile). We also note that several parameters important for modeling of oxygen diffusion and advection in the vasculature such as oxygen diffusivity, vessel wall oxygen permeability, and red blood cell radial density distribution and velocity are not known with sufficient accuracy and are the subject of continuous investigation.

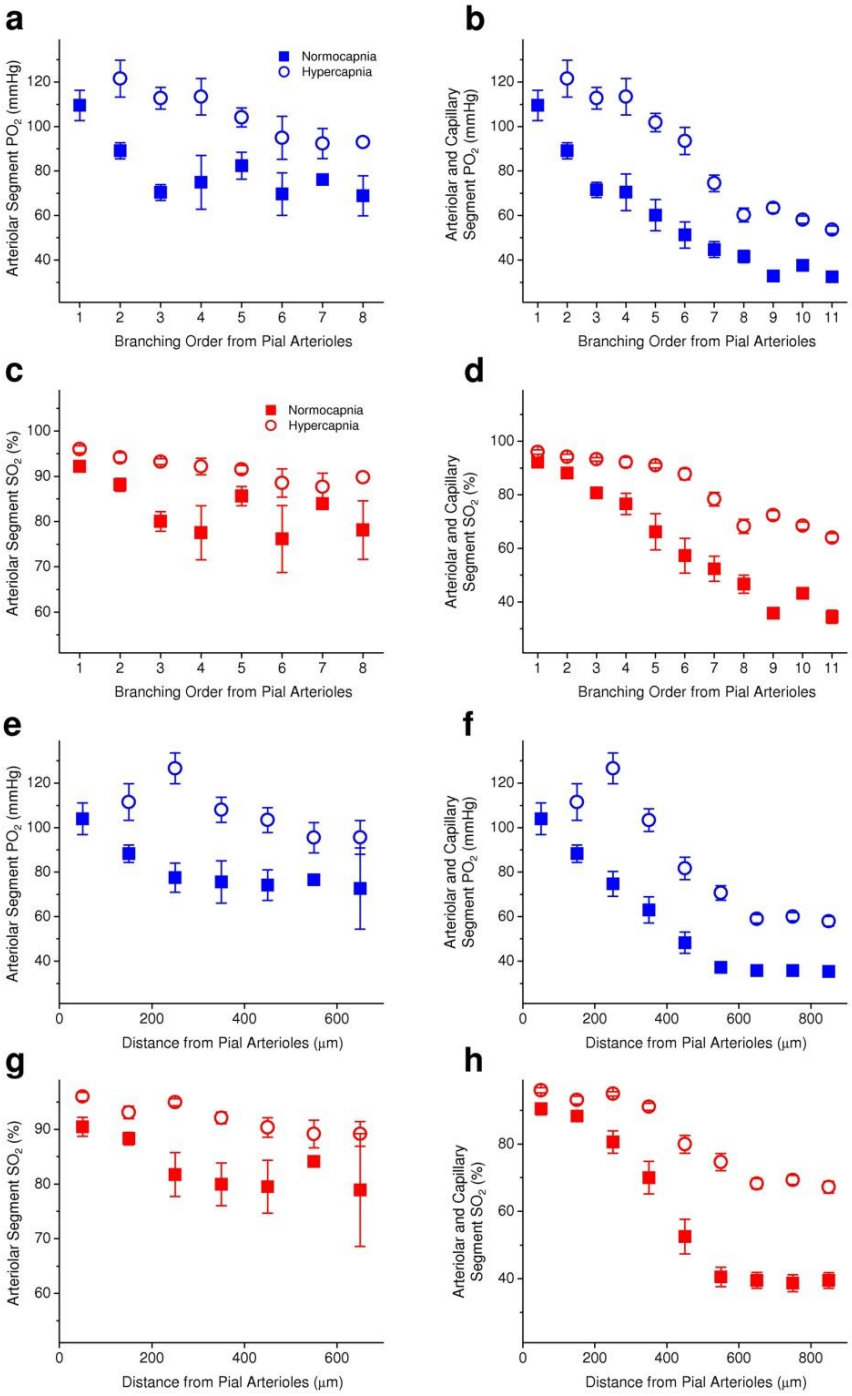

Supplementary Figure 3: Intravascular oxygen distribution as a function of branching order and distance from the pial arterioles. Mean vascular segment PO_2 and SO_2 dependence on the branching order and distance from the pial arterioles during normocapnia (solid symbols) and hypercapnia (empty symbols). (**a**,**c**,**e**,**g**) Arterioles only; arteriolar segments were traced starting from pial arterioles until reaching the capillaries. (**b**,**d**,**f**,**h**) Combined arterioles and capillaries; vascular segments (both arterioles and capillaries) were traced starting from pial arterioles until reaching the venules. The error bars in these graphs

are higher than in **Fig. 3**, indicating that intravascular arteriolar O_2 content correlates better with the vascular diameter than with the branching order and pathlength. Correlation of the O_2 content with the branching order and pathlength is further diminished for cortical venules due to their specific morphology, where both venular and capillary vascular segments of random calibers are frequently connecting to the larger venules. Data are expressed as mean ± s.e.m. and were estimated averaging over all vessels over all animals. *n* = 3 mice were used in each group.

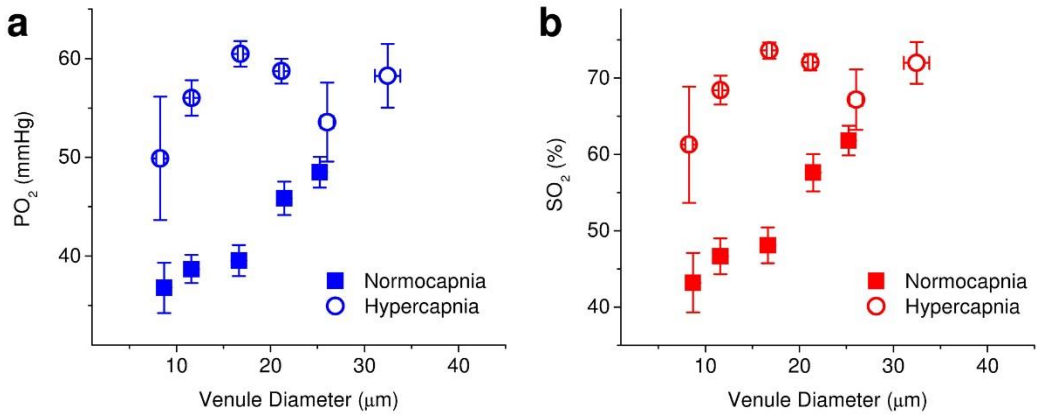

Supplementary Figure 4: Intravascular oxygen distribution in venules below the cortical surface. (**a**) Measured PO_2 in venules deeper than 100 µm from the brain surface as a function of the venules diameter during normocapnia (solid squares) and hypercapnia (empty circles). (**b**) SO_2 in venules deeper than 100 µm from the brain surface as a function of the venules diameter during normocapnia (solid squares) and hypercapnia (empty circles). Data are expressed as mean ± s.e.m. and were estimated averaging over all vessels over all animals. *n* = 3 mice were used in each group.

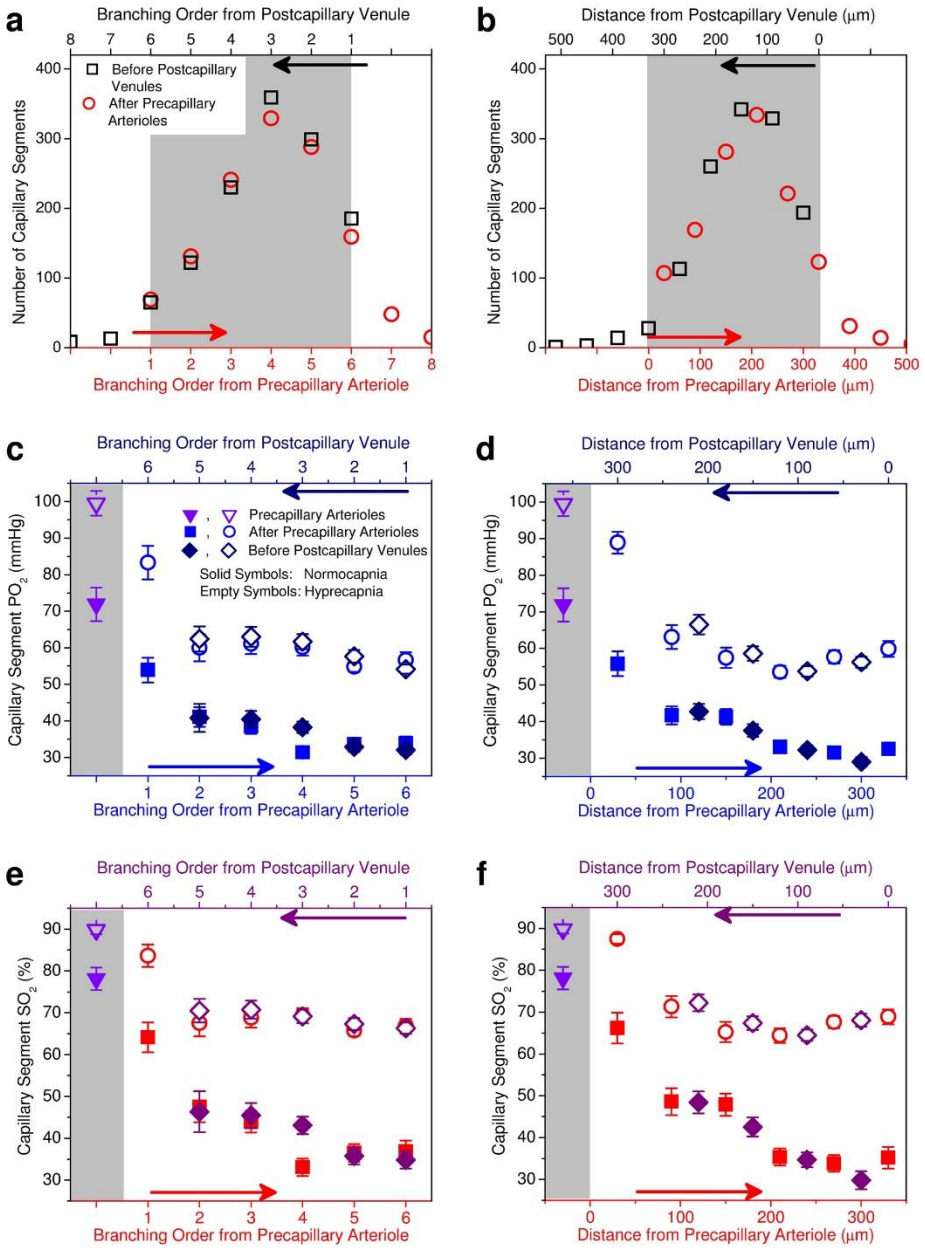

Supplementary Figure 5: Capillary segment number and oxygen content as a function of branching order and distance from the precapillary arterioles and postcapillary venules. (**a**, **b**) Histograms of the capillary segment number. We have found that each capillary segment is, on average, separated by 4.2 ± 1.6 capillary segments from the closest precapillary arteriole and 3.1 ± 1.5 capillary segments from the closest postcapillary venule, which resulted in the average number of segments in a capillary path = 6.3 (= 4.2 + 3.1 - 1, where -1 is for counting the segment in the middle twice). Similarly, we have found that center of each capillary segment is, on average, separated by 196 ± 95 μm from the closest precapillary arteriole and 147 ± 83 μm from the closest postcapillary venule, resulting in ~343 μm long average capillary pathlength between precapillary arteriole and postcapillary venule. In addition to capillary path analysis based on morphology only, by following the capillary paths along the blood flow

direction computed in the realistic microvascular networks, we estimated on average 5.9 ± 2.1 capillary branches and 364 ± 133-µm-long capillary pathlength between arterioles and venules (data are expressed as mean ± s.d.). Finally, an excellent match of the capillary segment histograms was obtained when capillary distributions calculated in two opposite directions from precapillary arteriolar and from postcapillary venular ends of capillary paths were overlapped over 6 branching orders (**a**) or 340 µm pathlength (**b**). Shaded areas in **a** and **b** represent the overlapping histogram regions in each panel. Therefore, we exploited the concept of an 'average capillary path' to overlap oxygenation measurements starting from both ends of capillary paths in **c**-**f**. (**c**-**f**) PO_2 and SO_2 inside the capillary segments. Solid and empty symbols in **c**-**f** represent normocapnic and hypercapnic measurements, respectively. Average PO_2 and SO_2 values in precapillary arterioles (purple triangle symbols) were plotted inside the shaded regions on the left hand side of the graphs. Finally, there was a good agreement between capillary segment PO_2 measurements at branching orders 2, 3, 4, 5, and 6 going downstream from the precapillary arterioles and capillary segment PO_2 measurements at branching orders 5, 4, 3, 2, and 1 going upstream from the postcapillary venules, respectively. This agreement further confirmed the observed capillary path morphology. Data in **c**-**f** are expressed as mean ± s.e.m. and were estimated averaging over all vessels over all animals. *n* = 6 mice were used for (**a**) and (**b**) and *n* = 3 mice were used for (**c**-**f**).

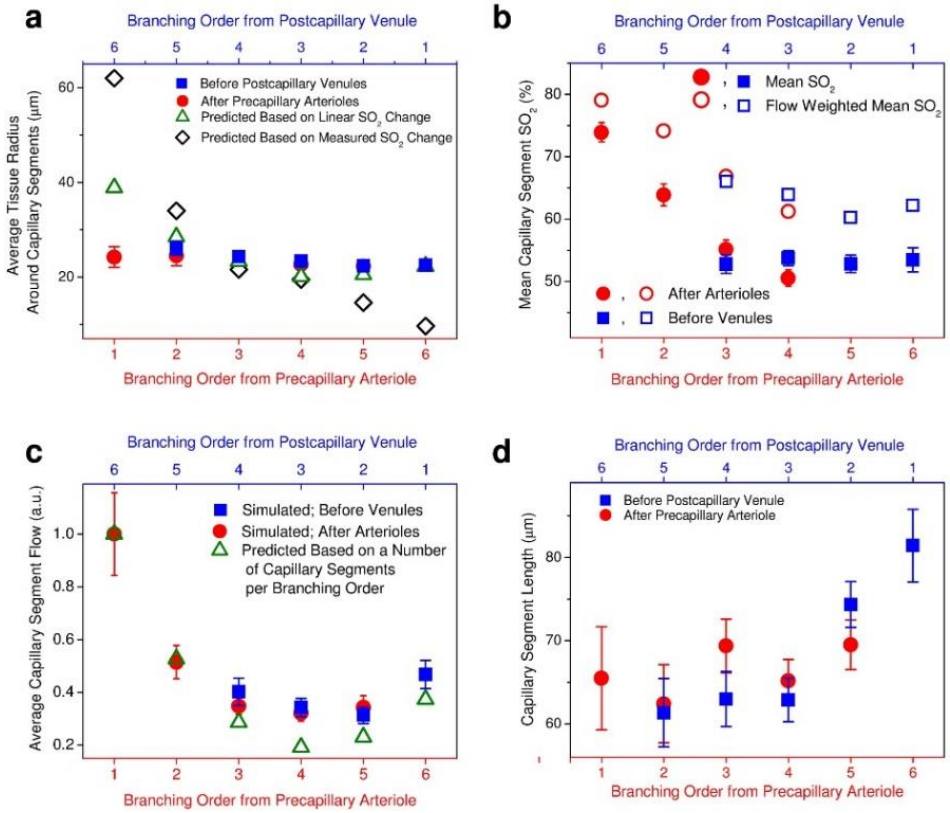

Supplementary Figure 6: Tissue territory separation by the capillary oxygen supply. (**a**) Average radius of the tissue cylinders supplied by the capillary segments as a function of the capillary branching order. Solid symbols represent cylinder radiuses estimated based on the measured distances between the tissue and the closest vascular segments. Volume of the tissue closest to a given vascular segment was deformed into a cylindrical tube around the vessel axis and the radius of the tissue cylinder was calculated. Empty black diamonds represent estimated tissue cylinder radiuses as a result of matching the average measured capillary SO_2 distributions during normoxia (**Fig. 4e**), while empty green triangles represent estimated tissue cylinder radiuses where the capillary SO_2 distribution was assumed to linearly decay along the capillary paths (ΔSO_2 =16% between precapillary arterioles and postcapillary venules). In both cases the radius estimation was performed by using the simulated capillary flow along the branching orders presented in **c**, while conserving the total tissue volume. (**b**) Simulated mean capillary SO_2 as a function of the capillary branching order after the precapillary arterioles (red circles) and before postcapillary venules (blue squares). Solid symbols represent mean SO_2 and empty symbols represent flow weighted mean SO_2. Significant discrepancy exists between flow-weighted mean SO_2 and mean SO_2 of the high branching order capillaries, while the shapes of the distributions are largely conserved. (**c**) Simulated average capillary segment flow as a function of the capillary branching order after precapillary arterioles (red circles) and before postcapillary venules (blue squares). Our simulations show that the average CBF at each capillary branching order approximately follows the inverse of the capillary number density (green triangles), as one would expect by the principle of mass conservation (i.e. capillary segment flow is proportional to the inverse number of capillaries per branch order presented in **Fig. 4a**). (**d**) Mean capillary segment

length as a function of the branching order after precapillary arterioles (solid circles) and postcapillary venules (solid squares). The average measured capillary segment length is 67.5 ± 1.4 μm. Data are expressed as mean ± s.e.m. and were estimated **a**: by averaging mean tissue radiuses from *n* = 6 mice; **b** and **c**: by averaging over all vessels over *n* = 3 mice, and **d**: by averaging mean capillary segment lengths from *n* = 6 mice.

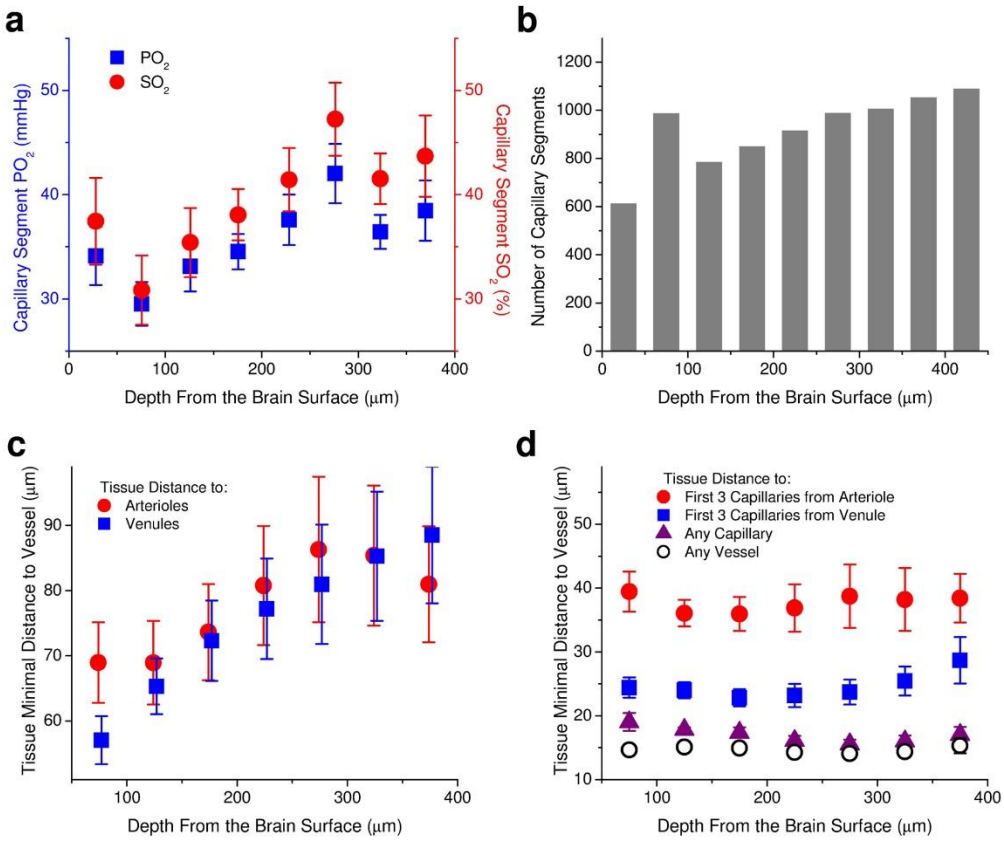

Supplementary Figure 7: Capillary oxygenation and spatial distribution as a function of depth. (**a**) Measured mean capillary PO_2 (solid squares) and SO_2 (solid circles) dependence on a depth from the brain surface. (**b**) Capillary density dependence on depth from the brain surface. A total number of capillaries from 6 microvascular stacks were reported for each 50-μm-thick depth region. An increase in the capillary density with depth correlates positively with a small increase in PO_2 vs depth in the upper 450 μm from the brain surface (**a**). A small PO_2 dip at ~75 μm depth in **a** coincides with an increased density of less oxygenated capillaries close to postcapillary venules in the same depth region (data not shown) that return the blood into venules after initial sprouting from the diving arterioles. (**c**) Tissue distance to the closest arteriole and venule as a function of depth. An increase in average tissue distance to arterioles and venules with increased depth correlates with the increase in tissue separation from the network of pial arterioles and veins. (**d**) Tissue minimal distance to the various microvascular segments shows a remarkably small variation as a function of depth. Red circles – distance to the capillaries within first three branching orders after the precapillary arteriole; blue squares – distance to the capillaries within last three branching orders before postcapillary venule; purple triangles – distance to any capillary; empty circles – distance to any vessel. In **a**, **c**, and **d** data are expressed as mean ± s.e.m for each 50-μm-thick depth section and were estimated **a**: by averaging over all vessels over n = 3 mice during normoxic normocapnia; **c** and **d**: by averaging the mean minimal distances from n = 6 mice.

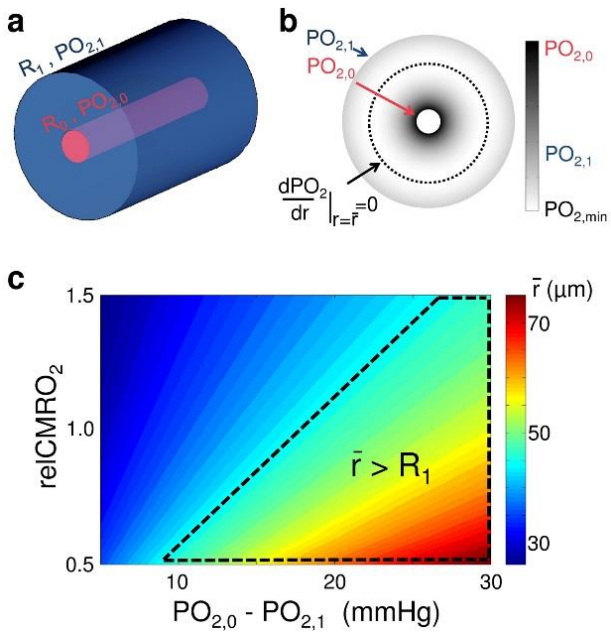

Supplementary Figure 8: Dependence of the supplied tissue territory size on the intravascular PO_2 and tissue $CMRO_2$. (**a**) Cylindrical tissue model. The inner cylinder represents a microvascular segment. (**b**) PO_2 distribution in the tissue cylinder. Dotted circle with radius $\bar{r}$ separates the tissue territories supplied by the inner and outer cylinders. (**c**) Map of $\bar{r}$ as a function of the relative $CMRO_2$ values and $PO_{2,1}$ – $PO_{2,0}$ differences, where $PO_{2,1}$ and $PO_{2,0}$ are partial oxygen pressures at the boundaries of the inner and outer cylinders, respectively.

Oxygen distribution in the brain tissue is governed by the PO_2 differences between oxygen sources (i.e. blood vessels) and tissue $CMRO_2$, such that 1) an increase in the PO_2 difference between two neighboring vessels in the absence of $CMRO_2$ change leads to an increase in the supplied tissue territory size around the vessel with the larger PO_2, and 2) an increase in $CMRO_2$ leads to an increase in the tissue territory supplied by the less oxygenated vessel and a simultaneous decrease in the territory supplied by the vessel with the higher PO_2. This somewhat less obvious dependence of the supplied territory sizes on $CMRO_2$ can be viewed as a consequence of the independence of the steady state diffusion equation solution (i.e. invariance of the solution spatial "shape") on $CMRO_2$ in a coordinate system in which the spatial dimensions are scaled by the diffusion length. Note that the diffusion length is proportional to $1/\sqrt{CMRO_2}$ and it represents the average distance from the O_2 source calculated along the straight line (e.g. "crow-flight length") along which the O_2 molecule diffuses before it gets utilized by the cells. As $CMRO_2$ increases and the diffusion length (scaling constant between dimensionless and real coordinate system) decreases, the *absolute reduction* in the tissue territory size is larger for the sources with higher PO_2.

An example is presented in the following text in which the above case of the isolated O_2 source is extended to illustrate the interaction of supplied tissue territories from several O_2 sources. We consider a simple cylindrical tissue model (**a**) where the inner cylinder represents a more oxygenated microvascular segment (e.g. precapillary arteriole or low branching order capillary) with the oxygen partial pressure $PO_{2,0}$ and radius R_0, and the outer cylinder with radius R_1

represents the continuum of the surrounding microvessels with the lower oxygenation ($PO_{2,1}$). If the tissue between two infinitely long concentrical cylinders has constant $CMRO_2$, then the steady state solution for the radial PO_2 distribution is given by

$$PO_2(r) = PO_{2,0} + \frac{CMRO_2}{4\alpha D}\left(r^2 - {R_0}^2\right) - \frac{CMRO_2}{2\alpha D}\bar{r}^2 \ln\frac{r}{R_0}\,, \quad (1)$$

where radius $\bar{r}$ separates the tissue territories supplied by the inner and outer cylinders (**b**). Radius $\bar{r}$ defines a circle represented by a dotted line where PO_2 gradient is zero (no diffusive oxygen flux across this circle) and it is given by

$$\bar{r} = \sqrt{\frac{R_1^2 - R_0^2}{2\ln(R_1/R_0)} + \frac{2\alpha D}{CMRO_2}\frac{(PO_{2,0} - PO_{2,1})}{\ln(R_1/R_0)}}. \quad (2)$$

According to Eq. (2), the radius $\bar{r}$ of the tissue territory supplied by the more oxygenated vessel increases with the increase in PO_2 difference and reduces with the increase in $CMRO_2$. Panel **c** shows that there is a large range of realistic $CMRO_2$ values and $PO_{2,1} - PO_{2,0}$ differences where the radius of tissue territory supplied by the inner vessel is larger than the radius of the outer cylinder, i.e. where the tissue territory of a more oxygenated vessel includes the less oxygenated vessel. The relative $CMRO_2$ values in **c** were computed in respect to $CMRO_{2,0}$ = 2 µmol O_2 cm^{-3} min^{-1}, and PO_2 values were selected within a measured capillary PO_2 range (**Fig. 4c**).

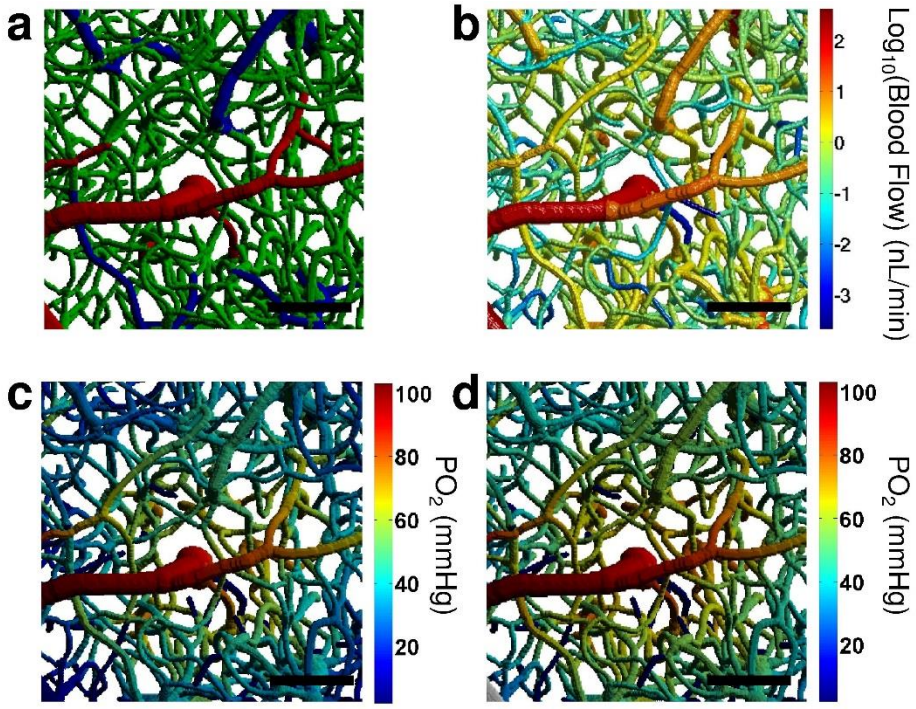

Supplementary Figure 9: Simulated CBF and PO_2 in a microvascular network. Examples of simulated CBF and PO_2 in the microvascular network at different $CMRO_2$. (**a**) Top view of the 450-µm-thick cortical microvascular stack with the labeled microvascular segments: arterioles (red), capillaries (green), and venules (blue). (**b**) Simulated CBF. (**c, d**) Simulated PO_2 for two different $CMRO_2$ values: $CMRO_2$ = 2.5 µmol cm^{-3} min^{-1} (**c**), and $CMRO_2$ = 1.5 µmol cm^{-3} min^{-1} (**d**). PO_2 values are color-coded and overlaid over microvascular structure presented in **a**. Scalebars: 100 µm.

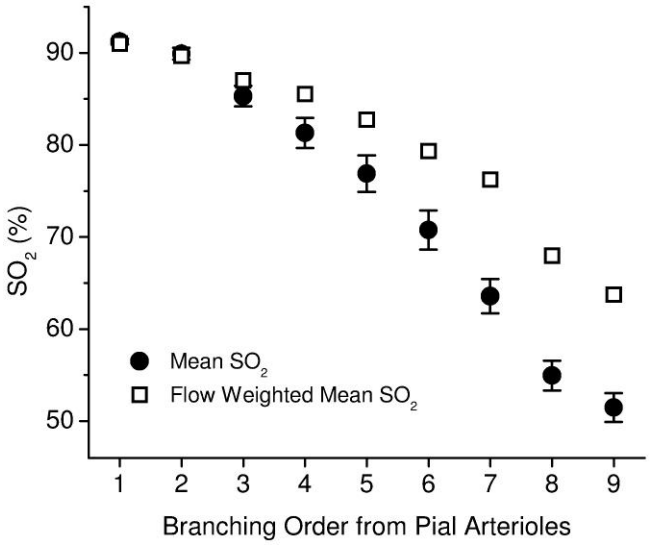

Supplementary Figure 10: Comparison of the mean SO_2 and flow-weighted mean SO_2 values. Simulated combined arteriolar and capillary mean (volume averaged) SO_2 values (solid circles; data are presented as mean ± s.e.m.) and flow weighted mean SO_2 (empty squares) dependence on a branching order from the pial arterioles. Vascular segments (both arterioles and capillaries) were traced starting from pial arterioles until reaching the postcapillary venules. Results were simulated from *n* = 3 mice.

Supplementary References

1. Kobayashi, H., Takizawa, N., Negishi, T. & Tanishita, K. Intravascular inhomogeneous oxygen distribution in microvessels: theory. Respir. Physiol. Neurobiol. **133**, 271-275 (2002).